JOURNAL OF AIRCRAFT
Vol. 35, No. 5, September–October 1998

Parallel Interaction of Incident Vortex Array with Oscillating Airfoil

Cheng-Hsiung Kuo* and J. K. Hsieh†
National Chung-Hsing University, Taichung 40227, Taiwan, Republic of China

Parallel interaction of an incident vortex array with a NACA 0012 airfoil in the form of sinusoidal oscillation was investigated experimentally, based on the concept of vorticity balance. It was found that the temporal–spatial variations of the local circulation can clearly reveal the convection of the highly distorted vorticity field over the airfoil. The phase-averaged near-surface flow structure confirmed that the temporal–spatial variations of the surface vorticity generation are closely related to the formation and subsequent motion of the leading-edge separation vortex along the airfoil. During the upstroke portion of the oscillation cycle, significant amounts of the surface vorticity were generated from the leading edge of the airfoil. The phase information of the local circulation relative to that of the surface vorticity generation clearly indicated that the leading-edge separation vortex was induced immediately after the passage of the clockwise-rotating incident vortex. When compared with the oscillating airfoil in uniform flow, the impingement of the incident vortex array on the oscillating airfoil increased the mean overall circulation around the airfoil over the oscillation cycle.

Nomenclature

C = root chord length of the airfoil, 12 cm
CV = local control volume
CT = contour enclosing each local control volume
$\mathrm{d}A$ = differential area within each control volume
f_e = oscillation frequency of the flat plate and airfoil
k = reduced frequency, $\pi f_e C/U_\infty$
Re_C = Reynolds number, $U_\infty C/\nu$
S = area enclosed by the boundary CT
T = period of the oscillation cycle, $1/f_e$
t = time, s
U_∞ = freestream velocity, 14 cm/s
$\bar{u}$ = mean streamwise velocity
u, v = streamwise and crossflow velocity components
$\mathbf{V}$ = velocity vectors
V_d = leading-edge separation vortex
VP = vorticity generation from the local surface of the airfoil
V_W = trailing vortex
V^+ = incident vortex of counterclockwise rotation
V^- = incident vortex of clockwise rotation
V^{+-} = combination of the distorted incident vortex
X, Y, Z = laboratory coordinate system
α_a = angle of attack of the oscillating airfoil
α_p = angle of attack of the oscillating flat plate
Γ_l = local circulation over the airfoil
Γ_o = overall circulation around the airfoil
λ = wavelength of the incident vortex array
$\boldsymbol{\omega}_z$ = out-of-plane vorticity vector in two-dimensional domain
$\langle\ \rangle$ = phase-averaged quantity
$*$ = nondimensional quantity

Introduction

THE generation of marked vibration as a result of large-amplitude and rapidly fluctuating loads on the airfoil[1,2] prompts one to investigate one of the most fundamental problems in the area of unsteady airfoil aerodynamics. The incident turbulence coming across the airfoil in turbomachinery, wind turbines, and the cyclic pitching of the helicopter rotor blades (or airfoils) represents some typical applications. The flow over the turbine or rotor blade is generally three dimensional, highly nonlinear, and unsteady in nature. The inflow speed (relative to the blade) along the span may range from the subsonic to transonic regimes. Furthermore, the characteristic length scale varying from the blade chord to the vortex size developed or passing over the blade can spread over several orders of magnitude.[3] All of the previously mentioned operational conditions magnify the complexity of the vortex/airfoil interaction and make the unsteady fluid dynamic problems on the airfoil extremely challenging.

McCroskey[4] reviewed the computational techniques and the latest advances in rotor-wake flow interactions. Nonlinear and unsteady characteristics pose a challenging problem in numerical modeling because they need time-consuming iterations. For the direct Navier–Stokes solver, different turbulence models can lead to quite different results.[5] Therefore, a suitable model should be validated to resolve the details of the flow structure because of the wide range of the operational conditions mentioned earlier. On the other hand, most experimental investigations were focused on understanding the flowfield by flow visualization and nonintrusive techniques. The surface pressure was measured and integrated over the airfoil to evaluate the aerodynamic performance. However, because of the complexity of the flowfield during interaction, a large number of experimental parameters cannot be taken into account equally, so that a comprehensive investigation of this problem is still lacking.

Previous studies on the vortex/blade interaction showed that the greatest surface pressure variation and intensive noise will be produced when the axis of the vortex filament is parallel to the span of the blade.[6,7] This is called the "parallel interaction." Despite the fact that the parallel interaction simplified the three-dimensional flow to a two-dimensional one, the validation of the simulated and experimental results was still limited to certain simplified cases. Interaction of the stationary two-dimensional airfoil with a single passing vortex filament was first investigated for its simplicity. Several investigations on this aspect were the experimental results from Booth and Yu[8] and Horner et al.[9] at a low Reynolds number, the inviscid simulation of Srinivasan and Baeder[10] for transonic flow, and

---

Received Oct. 16, 1997; revision received April 30, 1998; accepted for publication May 8, 1998.

*Professor, Department of Mechanical Engineering.

†Graduate Assistant, Department of Mechanical Engineering.

the panel method by Mook and Dong.[11] The severity of the vortex/blade interaction was found to depend strongly upon the strength of the incident vortex and the relative height of the incident vortex above the blade.[9] In addition, it is important for the airfoil to oscillate near the stalled angle of attack (AOA) because the associated aerodynamics will affect the stall boundaries. Although significant progress had been made to understand the onset and formation of dynamic deep-stall during the past few decades,[12] the choices of the turbulence models, numerical schemes, grid spacing, and artificial viscosity all contribute to the differences between the computational and experimental results, even in the two-dimensional flows. These choices are even more critical in the light stall condition because a proper unsteady transition model is not available at this time. Therefore, an understanding of the underlying flow physics relies mainly on the experimental work in this aspect.

A related study was performed by Gopalkrishnan et al.[13] investigating the oscillating airfoil interacting with an incident wake behind a cylinder. By direct force measurement and flow visualization they concluded that the thrust efficiency of the oscillating airfoil is a strong function of the phase difference between the oscillating airfoil and the arrival of the incident wake. However, no information is provided to illustrate the associated vortical structure above the airfoil. In the current study, parallel interaction of the incident vortex array with the sinusoidally oscillating airfoil (NACA 0012), within the regime of light stall ($\alpha = 10$–20 deg), will be investigated by experiments based on the concept of vorticity balance. Moreover, the modified phase-averaged technique is used to investigate the unsteady flow structures over the airfoil within the oscillation cycle. The local circulation and vorticity generation from the airfoil surface are evaluated from the phase-averaged flowfield. The intention, motivated by the work of Gopalkrishnan et al.,[13] is to provide insight into the flow physics of the distorted vorticity field over the airfoil interacting in parallel with an incident vortex array. Furthermore, the ideas and techniques used in the present study are presented as a first step toward the design of experiments intended to simulate helicopter blade dynamic stall and blade/vortex interaction.

Experimental Conditions and Methods

Flow Conditions

The experiments were performed in a recirculating water channel with test section dimensions of 50 × 40 × 240 cm. The flow nonuniformity was around 1.2%, based on the difference between the maximum and the minimum freestream velocity in the test section. The NACA 0012 airfoil had a root chord length of 12 cm. The Reynolds number, based on the root chord of the airfoil, was around 4.0×10^4. Fluorescent sodium and Rhodamin B are used as tracers in conjunction with the laser-sheet technique for flow visualization. The tracers are supplied by a constant, but low, head feeder. The incident vortex array can be visualized while the dye is issued naturally from the trailing end of the upstream oscillating flat plate. Furthermore, dyes of different colors are issued naturally from both the leading and trailing edges of the airfoil to show the interaction of the incident vortex array with the oscillating airfoil.

The incident vortex array is generated by a thin flat plate oscillating sinusoidally about zero AOA at high reduced frequency ($k = 6.67$) and small amplitude (± 3 deg). At these conditions the wake behind the upstream oscillating flat plate forms an in-line vortex array.[14] The upstream flat plate and the downstream airfoil are oriented horizontally and are arranged in tandem (no offset in crossflow direction) at a depth of 25 cm below the water-free surface. They have the same chord length and their leading edges are three root chords ($3C$) apart. This distance allows an incident vortex having a clockwise rotating sense to first arrive at the leading edge of the airfoil when the AOA is at $\alpha = 10$ deg. Their pivoting axes are located at one-third of the chord ($C/3$). As depicted in Fig. 1, the pitching oscillations of the flat plate and the airfoil are driven by two identical simple-harmonic-motion mechanisms. These two mechanisms are positively linked through the toothed V-belt without slippage. With this design the upstream flat plate and the downstream airfoil can oscillate at the same reduced frequency k, but at different amplitudes. The oscillating amplitude can be adjusted independently by varying the eccentricity on the individual rotating disk. The instantaneous AOA of the upstream flat plate is $\alpha_p(t) = 0 + 3$ deg $\sin(2\pi f_e t)$, while that of the downstream oscillating airfoil is $\alpha_a(t) = 15 + 5$ deg $\sin(2\pi f_e t)$. In the present study, the oscillation of the upstream flat plate is controlled in phase with that of the downstream airfoil. The flat plate and the airfoil begin their oscillations from their minimum AOA.

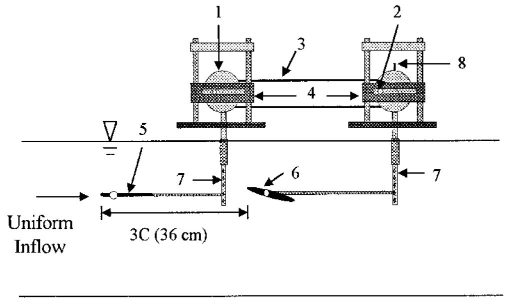

Fig. 1 Experimental setup for generation of the incident vortex array and interaction with the oscillating airfoil. 1, rotating disks; 2, eccentric pin; 3, driving V-belt; 4, sliding bars; 5, upstream oscillating flat plate; 6, downstream oscillating airfoil; 7, connecting rod from sides; and 8, triggering piece.

Velocity Measurements

Above the airfoil, the velocity field was measured by the laser Dopper velocimetry (LDV) system together with a precise traversing table having 0.01 mm accuracy. The laser Doppler anemometry (LDA) system contains an argon ion laser source, a Bragg cell for frequency shifting, and integrated fiber-optic detecting and receiving modules. By using a beam expander, the size of the measuring volume is 0.043 mm in diameter and 0.51 mm in length. Furthermore, proper seeding concentration and small size (8 μm) of the seeding particles (TiO_2) give a response time of 6.2 μs. Relative to the time scale in the flowfield, the sufficiently fast response time of the seeding particles in the water flow indeed produces continuous time signals for LDV velocity measurement. A correlation-based signal processor is employed to validate the data by successfully detecting eight cycles within each Doppler burst. The standard deviation of velocity measurement in the uniform stream is around 0.42%. With acceptable beam-surface interference, the measuring location can be placed as close as 0.3 and 1.0 mm to the airfoil surface for the streamwise and transverse velocity measurements, respectively. Within this near-surface region, the validated data rate is around 500–700/s, leading to a maximum uncertainty of 5.37% of the local velocity. Before entering the data-acquisition system, all of the validated velocity time signals are fed into a low-pass filter having 100-kHz bandwidth to avoid aliasing.

On the plane at the midspan ($Z = 0$), the velocity vectors were measured at 12 stations, ranging from $X/C = -0.083$ to $X/C = +1.083$ over the airfoil as depicted in Fig. 2. Here X, Y, and Z represent the laboratory coordinate system with origin at the airfoil's nose. The magnitude of the velocity reaches the freestream velocity beyond $Y/C = \pm 0.4$. However, the upper and lower boundaries of the velocity measurements are extended to $Y/C = \pm 1.5$ to include all of the vorticity. At each measuring location the total sampling time of each velocity measurement is 40.96 s, including about 102.4 cycles of oscillation. Relative to the dominant frequency in the flowfield (around 2.5 Hz), the choice of a high sampling frequency (100

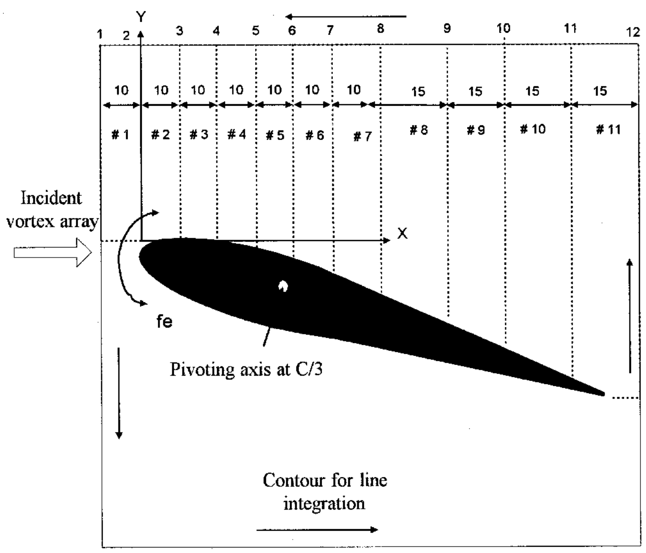

Fig. 2 Definition of the control volumes to evaluate overall circulation around the airfoil (solid-line contour) and local circulation at various streamwise locations over the airfoil (dashed-line contours).

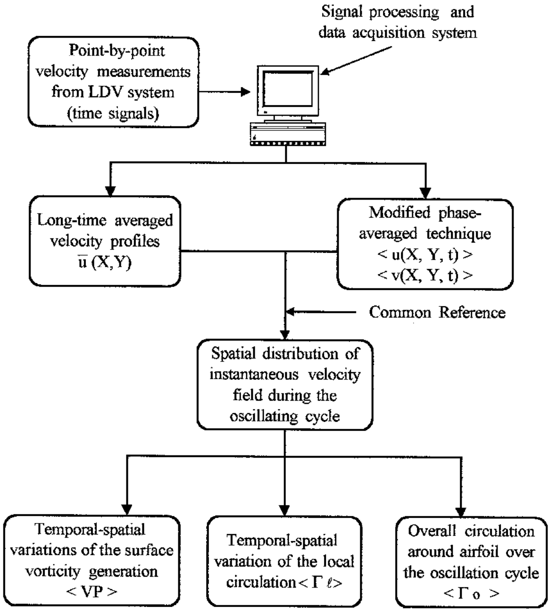

Fig. 3 Sequence of postprocessing technique to evaluate the averaged value and phase-averaged physical quantities in the flowfield.

Hz) and long sampling time (40.96 s) will satisfy the temporal resolution requirement of the velocity measurements. There are around 520 measuring points above the airfoil to provide sufficient spatial resolution.

Postprocessing of Velocity Data

The postprocessing sequence of the velocity data is depicted in Fig. 3. The time histories of the velocity signals from the LDV system are first acquired by the personal-computer-based data-acquisition system. This system includes a 12-bit A/D conversion interface with programmable sampling rate up to 330 kHz and sample-and-hold characteristic. The data acquisition is initiated by a triggering unit (an optical interrupter) located on the edge of the rotating disk (Fig. 1) to generate a triggering pulse. This triggering pulse will provide the common reference for all of the velocity measurements that commence when the oscillating airfoil arrives at $\alpha = 10$ deg. In this study the maximum variation of the oscillation period is about $0.34\%T$. This ensures the periodicity of the flow and the suitability of applying the modified phase-averaged technique.[15]

At each measuring location within the flowfield, the velocity measured by the LDV system represents only the temporal variation of the local velocity. At any instant within the oscillation cycle, the phase-averaged velocity field [$\langle u(X, Y, t)\rangle$ and $\langle v(X, Y, t)\rangle$] can be reconstructed by the modified phase-averaged technique using the triggering pulse as common reference. Note that the phase-averaged technique averages the cyclic data points over 100 cycles. The temporal resolution is determined by the sampling rate (100 Hz), equivalent to 45 instants within the complete oscillation cycle. Subsequently, the phase-averaged local circulation $\langle \Gamma_l^* \rangle$ around each local control volume (bounded by the dashed-line contours in Fig. 2) and the overall circulation $\langle \Gamma_o^* \rangle$ around the airfoil (bounded by the solid-line contour in Fig. 2) are all evaluated by line integration along their boundaries. The circulation is defined as positive, when the rotation is counterclockwise. The phase-averaged vorticity generation $\langle VP^* \rangle$ from the airfoil surface, the local circulation $\langle \Gamma_l^* \rangle$, and the overall circulation $\langle \Gamma_o^* \rangle$ around the airfoil are all processed to explore the flow characteristics over the oscillating airfoil. More details of the postprocessing schemes for performing the vorticity balance on each local control volume can be found in Hsieh.[16]

Results and Discussion

Incident Flow Structures of In-Line Vortex Array

In Fig. 4 the phase-averaged and mean streamwise velocity profiles of the incident vortex array are measured at $X/C = -1.0$ to illustrate the incident flow structure. All of the abscissas in Fig. 4 are normalized by the freestream velocity. In

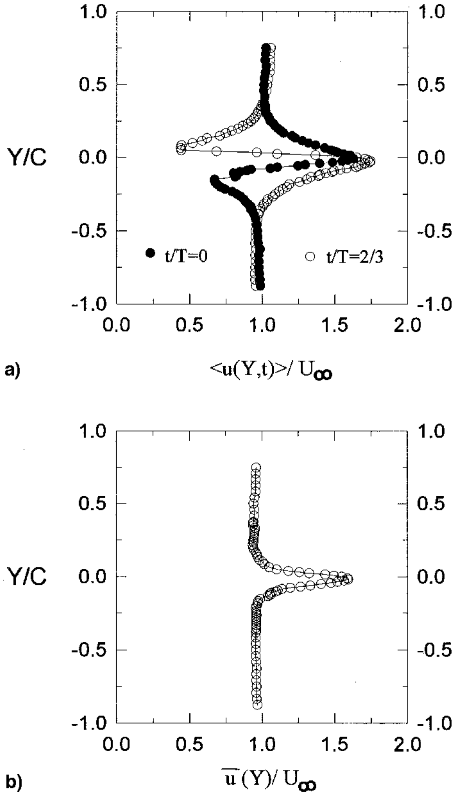

Fig. 4 Typical streamwise velocity profiles measured at $X/C = -1.0$ for a) phase-averaged velocity profiles at two different instants within the oscillation cycle and b) long-time averaged velocity profile.

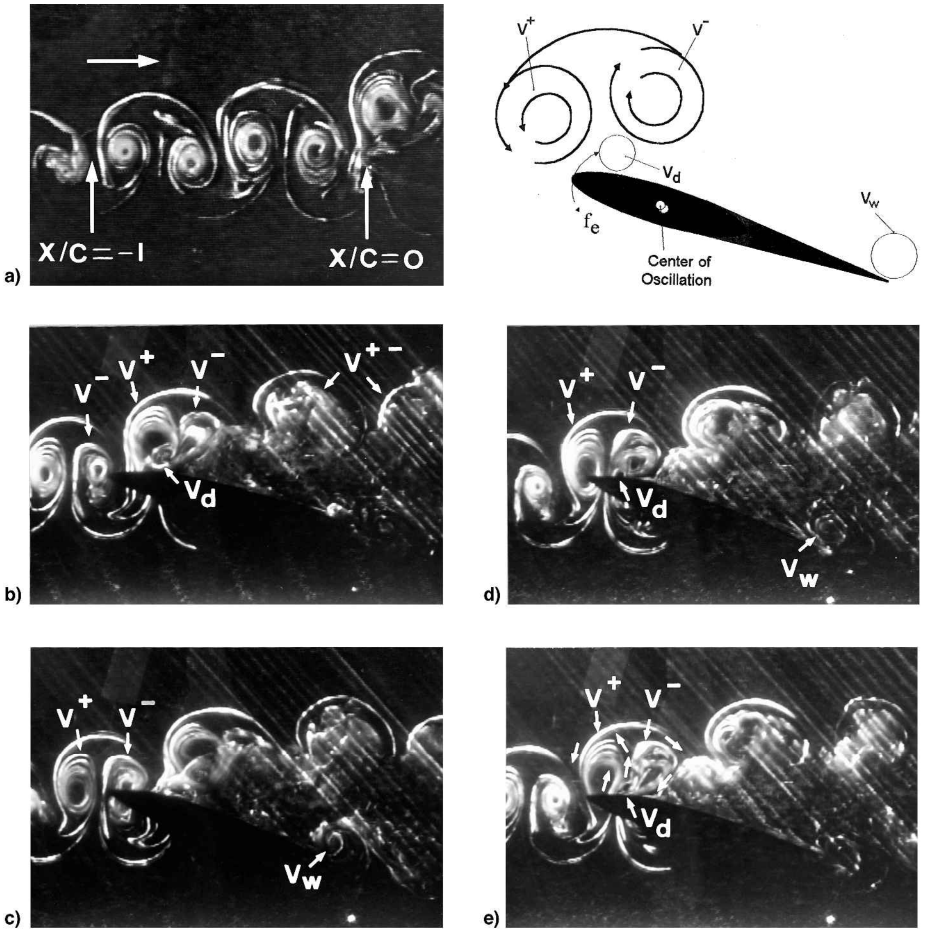

Fig. 5 Flow patterns for a) the incident vortex array and for vortex/airfoil interacting flow structures over the airfoil at selected instants within the oscillation cycle, b) $t/T = 0$ ($\alpha = 10$ deg ↑), c) $t/T = 2/6$ ($\alpha = 16.7$ deg ↑), d) $t/T = 4/6$ ($\alpha = 16.70$ deg ↓), and e) $t/T = 5/6$ ($\alpha = 13.3$ deg ↓).

Fig. 4a, the phase-averaged velocity profiles $\langle u(Y, t)\rangle$ show antisymmetric distributions about $Y/C = 0$ at two different instants ($t/T = 0$ and $t/T = 2/3$) within the oscillation cycle. Two local maxima of each $\langle u(Y, t)\rangle$ distribution are situated very close to the location $Y/C = 0$, where significant velocity gradients $\langle \partial u(X, Y, t)/\partial Y\rangle$ occur. The highly sheared velocity profile near $Y/C = 0$ clearly signifies the dominant vorticity field within this region. In addition, the velocity profile at $t/T = 0$ is almost π out of phase when compared with that at $t/T = 2/3$. This result reveals that the vorticity field of the incident vortex array will switch its sign alternately within the oscillating cycle. The results of Fig. 4a imply that the incident vortex array forms an in-line arrangement near $Y/C = 0$, having vorticity of alternating sign. The results in Fig. 4a correlate well with the flow patterns in Fig. 5a. Upstream of the oscillating airfoil the trajectory (or center) of the incident vortex array shown in Fig. 5a is located approximately along $Y/C = 0$. However, it is deflected slightly upward when the leading edge of the oscillating airfoil is encountered.

Furthermore, the distribution of $\bar{u}(Y)$ in Fig. 4b shows a jet-like flow profile with the maximum overshoot of $1.6U_\infty$ located at $Y/C = 0$. This jet-like distribution $\bar{u}(Y)$ of the incident vortex array had been confirmed by Koochesfahani,[14] who studied the flow patterns behind a flat plate oscillating at high reduced frequency. As shown in Fig. 5a, the incident vortex array has a wavelength $\lambda \approx C/2$ and moves with a speed $1.13U_\infty$ along the direction parallel to the freestream. In the current study, the convection speed ($1.13U_\infty$) obtained by qualitative estimation from flow visualization (Fig. 6a) is consistent with that of Booth and Yu[8] ($1.18U_\infty$). A related study on the high Mach number circular jet issuing into a quiescent environment showed that the convection speed of the coherent vortex structure is around 0.55–0.6 times the jet centerline velocity.[17] The estimated convection speed of the incident vortex array based on the results of Ho and Nosseir[17] is about 15% higher, most likely because of the high Mach number in the circular jet.

Interacting Vortex Structure Above the Airfoil

General flow patterns of the vortex/airfoil interaction are shown in Figs. 5b–5e for selected instants within the oscillation cycle. In the inset of this figure V^+ and V^- denote the counterclockwise and clockwise rotating vortices of the incident vortex array, respectively, V_d represents the leading-edge separation vortex with a clockwise sense of rotation, and V_W denotes the trailing vortex with a counterclockwise sense of rotation. V^{+-} represents the mushroom vortex that is the combination of the distorted V^+ and V^- vortices over the airfoil. The sequential photographs in Figs. 5b–5e clearly show that the vortices V^+ and V^- arrive alternately at the leading edge of the airfoil within the oscillating cycle. Note that $t/T = 0$ defines the instant when the AOA of the airfoil is $\alpha = 10$ deg (Fig. 5b). In Fig. 5c, the V^- arrives at the leading edge of the airfoil at $t/T = 2/6$ (or $\alpha = 16.7$ deg ↑), experiencing severe distortion. Then, at $t/T = 4/6$ (or $\alpha = 16.7$ deg ↓), the birth of V_d is discernible immediately behind the preceding vortex V^-, and is located closely adjacent to the surface near the leading-edge region (Fig. 5d). Subsequently, in Figs. 5e and 5b, V_d continues to grow in size, and is lifted away from the surface because of the mutual induction from both the following V^+ and the preceding V^- vortices. This can be referred to with the arrows indicated in Fig. 5e.

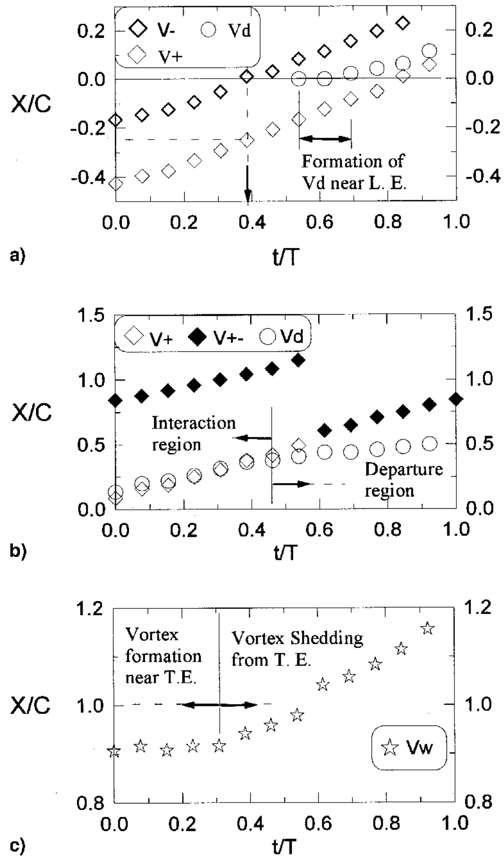

Fig. 6 Vortex trajectories for a) V_d, V^+, and V^-; b) V_d, V^{+-}, and V^+; and c) V_w over the airfoil within one complete cycle of oscillation.

Within the oscillation cycle the trajectories (or center) of each vortex structure above the airfoil are shown in Fig. 6. All of the data points in Fig. 6 are obtained from the flow visualization results over 52 oscillating cycles, having a maximum deviation of around 1.21%. Upstream of the airfoil the trajectories of the incident vortices V^+ and V^-, shown in Fig. 6a, are parallel to each other and a streamwise distance $C/4$ apart. This result confirms that the incident vortex array has a half-wavelength $\lambda/2 \approx C/4$, which agrees with the flow patterns observed in Fig. 5a. Within the region $X/C \leq 0$ in Fig. 6a, the approximate constant slopes of these trajectories imply that the incident vortex array upstream of the airfoil moves at a nearly constant speed ($1.13U_\infty$) in the streamwise direction. At $t/T = 0.38$ in Fig. 6a, the V^- vortex first arrives at the leading edge of the airfoil. At a later instant $t/T = 0.55$, V_d is observed near the leading-edge region (the open circles around the horizontal solid line in Fig. 6a). Within the time interval $0.55 < t/T < 0.70$ of Fig. 6a, the approximate zero slope of the trajectory of V_d is indicative of the formation stage of this vortex. The trajectories of V_d and V^+ merge gradually together within $0.70 < t/T < 0.95$ of Fig. 6a, and coincide with each other within the interval $0 \leq t/T \leq 0.45$ of Fig. 6b. This evidence clearly indicates that V_d has been lifted by and becomes part of the vortex V^+. In Fig. 6a, the lifting process of V_d gives a lower convection speed ($0.89U_\infty$) within the time interval $0.70 < t/T < 0.95$. However, in the interacting region of Fig. 6b, V_d interacts strongly with and becomes part of V^+, moving at a higher speed ($1.13U_\infty$) during the time interval $0 < t/T < 0.45$. In the departure region of Fig. 6b ($t/T \geq 0.45$), the trajectories of the vortices V^+ and V_d start to deviate. The speed of the vortex V_d slows down, whereas that of the distorted vortex V^+ stays unchanged. Around $X/C = 0.5$ in Fig. 6b, the trajectory of V^+ continuously merges into that of V^{+-}, that represents the combination of the distorted V^+ and V^- vortices over the airfoil. The positive slope for V^{+-} clearly indicates that the distorted incident vortex array moves downstream with a nearly constant speed along the airfoil.

In Fig. 6c, within $0 < t/T < 0.3$, the trajectory of V_W has zero slope, indicating the formation stage of the trailing vortex near $X/C = 0.9$. During this stage the trailing vortex continuously accumulates vorticity of counterclockwise sense and further increases in strength. V_W starts to shed into the wake at around $t/T = 0.3$ with a slower speed ($0.52U_\infty$) within $0.9 < X/C < 1.0$, and then at a higher speed ($0.88U_\infty$) downstream of the trailing edge ($X/C > 1.0$). As a result of shedding the counterclockwise vorticity into the wake of the airfoil, the overall circulation around the airfoil is expected to increase for $t/T \geq 0.3$. The remarkable finding is that the departure region ($t/T > 0.45$) in Fig. 6b begins shortly after the instant ($t/T = 0.3$) at which the trailing vortex starts to shed. This suggests that the trajectory (or the motion) of V_d is affected by the formation and shedding of V_W.

Local Circulation over the Airfoil

Within the oscillation cycle, evolution of the vortex structures over the airfoil is best described by the presentation of vorticity contours over the airfoil. However, vorticity measurement over the entire flowfield is extremely time-consuming when the LDV system is employed. In the current study, the concept of local circulation[18] is employed to illustrate the time-dependent characteristics of the distorted vorticity field over the oscillating airfoil. For a two-dimensional flowfield, the line integral of all the velocity vectors around each closed contour can represent the local circulation, which equals the total spanwise vorticity integrated within the area bounded by the closed contour:

$$\langle \Gamma_l(X, t)\rangle = \oint_{CT} \langle \boldsymbol{V}(X, t)\rangle \cdot \mathrm{d}\boldsymbol{l} = \int_S \langle \omega_z(X, t)\rangle \cdot \mathrm{d}A \qquad (1)$$

The quantities in the brackets represent the phase-averaged values. By inspecting the size of the vortices in the flow visualization results, 11 control volumes (enclosed by the dashed-line contours shown in Fig. 2) are selected to resolve the streamwise evolution of the vortex structures over the airfoil. Meanwhile, the velocity vectors are measured along the boundaries of each control volume to evaluate the local circulation by line integration.

Temporal variations of nondimensional, phase-averaged local circulation $\langle \Gamma_l^*(X, t)\rangle = 2\langle \Gamma_l(X, t)\rangle/U_\infty C$ are shown in Fig. 7 for each local CV located at successive X/C locations over the airfoil. As indicated in Fig. 7, the horizontal dashed lines denote the zero circulation level. The maximum deviation estimated over 100 cycles is about 1.71%. The magnitude of $\langle \Gamma_l^*(X, t)\rangle$ is indicative of the strength of the integrated vorticity field within each local CV. The magnitude of $\langle \Gamma_l^*(X, t)\rangle$ is positive while the integrated vorticity field having counterclockwise sense passes by or resides in each local CV, and vice versa. For the attached two-dimensional flow, the vorticity generation from the airfoil surface cancels exactly the net vorticity flux into and out of each CV. Thus, the temporal variation of the local circulation within each CV will be scaled with the velocity change of the periodic incident vortex array.[18] This agrees with the results shown in the region $0 \leq X/C \leq 0.083$ of Fig. 7, in which the magnitude of $\langle \Gamma_l^*(X, t)\rangle$ reaches a positive maximum at $t/T = 0.10$ and a negative minimum at $t/T = 0.8$. At these two instants the maximum and minimum values of $\langle \Gamma_l^*(X, t)\rangle$ indicates the residence of the vortices V^+ (between Figs. 5b and 5c) and V^- (Fig. 5e) within this CV. In the $0 < X/C < 0.333$ region of Fig. 7, the increasing magnitude of the local negative minimum of $\Gamma_l^*(X, t)\rangle$ is accompanied by a decreasing magnitude of the local positive maximum. This change is caused primarily by the formation and subsequent

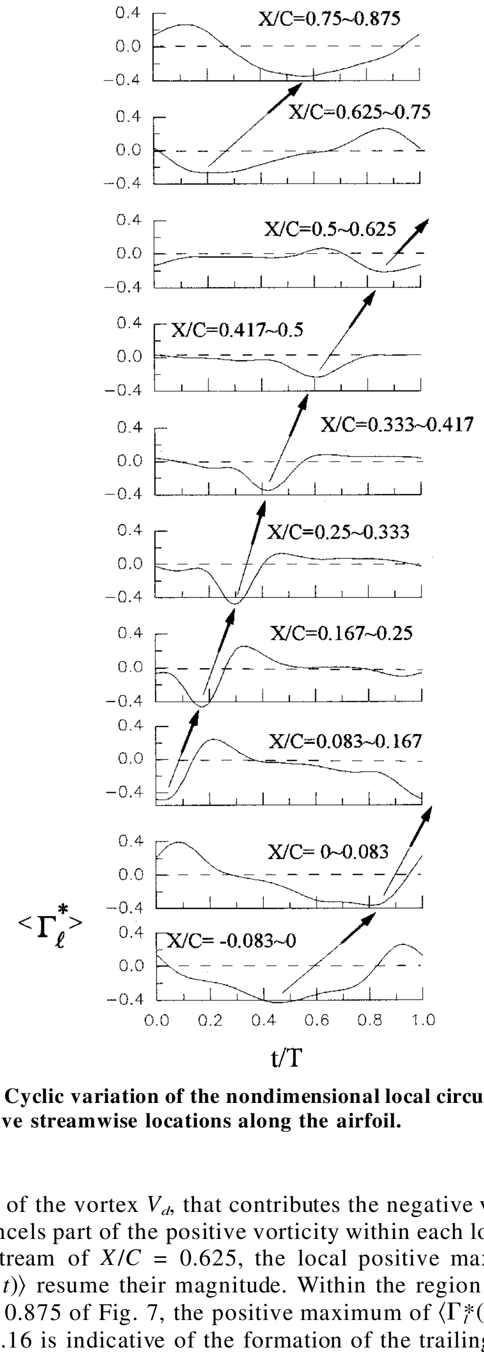

Fig. 7 Cyclic variation of the nondimensional local circulation at successive streamwise locations along the airfoil.

motion of the vortex V_d, that contributes the negative vorticity and cancels part of the positive vorticity within each local *CV*. Downstream of $X/C = 0.625$, the local positive maxima of $\langle\Gamma_l^*(X, t)\rangle$ resume their magnitude. Within the region $0.75 \leq X/C \leq 0.875$ of Fig. 7, the positive maximum of $\langle\Gamma_l^*(X, t)\rangle$ at $t/T = 0.16$ is indicative of the formation of the trailing vortex V_W (Fig. 6c).

The arrows, connecting all of the negative minima of $\langle\Gamma_l^*(X, t)\rangle$ at successive X/C locations, show the downstream movement of the clockwise vorticity field along the airfoil. The slopes of these arrows denote the local speed at which the distorted vorticity field is moving. A similar trend can also be found for the counterclockwise vorticity field by connecting the local positive maxima of $\langle\Gamma_l^*(X, t)\rangle$ at successive X/C locations. Evidently, slightly upstream of the leading-edge region ($-0.083 < X/C < 0$), the convection slows down ($0.39U_\infty$) because the incident vortex array is distorted by the presence of the airfoil. Note that the convection speed of the incident vortex array upstream of the airfoil is around $1.13U_\infty$. Within the $0 < X/C < 0.5$ region, the convection speed resumes its magnitude ($1.21U_\infty$)), implying a slight acceleration of the incident vortex flow in this region. This accelerating characteristic within $0 < X/C < 0.5$ is similar to that measured by Booth and Yu.[8] Downstream of $X/C = 0.5$, the convection of the vorticity field over the airfoil is retarded ($0.74U_\infty$) because it interacts with the low-speed thickened boundary-layer flow.

Local Surface Vorticity Production

Vorticity balance on any two-dimensional local CV can be expressed as

$$\frac{d\langle\Gamma_l\rangle}{dt} = \int \langle u\rangle\langle\omega_z\rangle \, dY\Big|_{in} - \int \langle u\rangle\langle\omega_z\rangle \, dY\Big|_{out} - \nu \int \frac{\partial\langle\omega_z\rangle}{\partial Y}\bigg|_{wall} dX \qquad (2)$$

All of the quantities in brackets represent the phase-averaged values. Equation (2) simply states that the time rate of change of the local circulation can be balanced by the net vorticity flux across the local control surfaces (the first and the second terms) and the local vorticity generated from the surface of the airfoil (the last term). In the present study, the time rate of change of the local circulation is obtained by direct differentiating the local circulation with the central difference scheme, having errors order $(\Delta t)^4/30$. The vorticity $\langle\omega_z\rangle$ at the measuring location along the inlet and the outlet of each *CV* is evaluated by the definition $\langle\omega_z\rangle = (\oint \langle v\rangle \cdot dc)/\Delta A$. Here, ΔA is the area of each cell enclosed by four neighboring grids of the velocity measurements. Therefore, the net vorticity flux is calculated simply by performing the integration $\int \langle u\rangle\langle\omega_z\rangle \, dY$ at the inlet and outlet of each *CV*. Subsequently, the phase-averaged vorticity generation from the local surface is computed by subtracting net vorticity flux across local control surfaces from $d\langle\Gamma_l\rangle/dt$. More details of the postprocessing schemes can be found in Hsieh.[16] The nondimensional phase-averaged vorticity generation is defined as $\langle VP^*\rangle = -(4\pi/Re_c k) \int (\partial\langle\omega_z^*\rangle/\partial Y^*)|_{wall} \, dX^*$. The temporal variations of $\langle VP^*\rangle$ at succes-

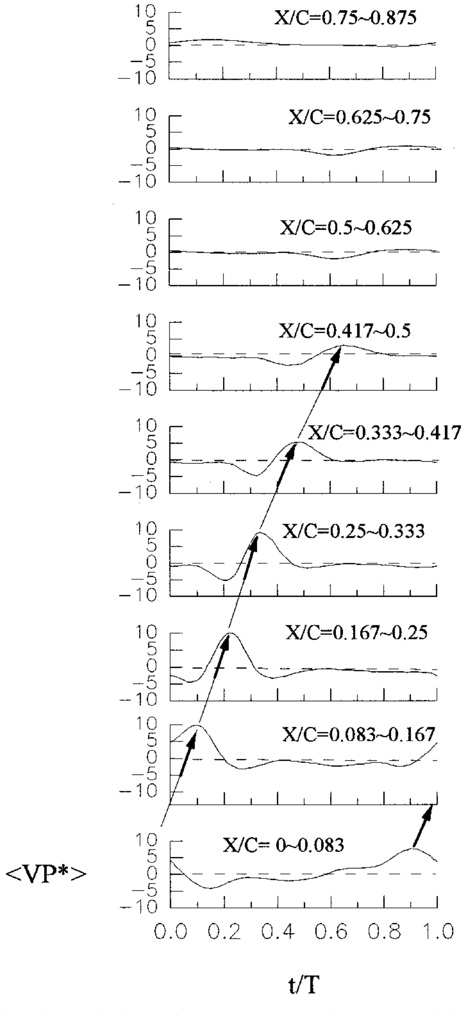

Fig. 8 Cyclic variation of the nondimensional vorticity generation at successive streamwise locations above the airfoil.

sive streamwise locations over the airfoil are shown in Fig. 8. The maximum uncertainty of $\langle VP^* \rangle$ estimated over 100 cycles is around 2.17%. The horizontal dashed-line on each plot indicates the zero level of vorticity generation. It is found that within the range $0 \leq X/C \leq 0.5$ in Fig. 8, the temporal variations of $\langle VP^* \rangle$ are characterized by a summit-like distribution. The ascending portion of the summit-like distribution of $\langle VP^* \rangle$ implies that the near-surface velocity profiles will change following the G sequence shown in the inset of Fig. 9. On the contrary, the descending portion of the summit-like distribution of $\langle VP^* \rangle$ indicates that the switch of the near-surface velocity profiles will follow the H sequence in the inset of Fig. 9.

Near the leading-edge region ($0 < X/C < 0.083$), the magnitude of $\langle VP^* \rangle$ becomes positive after $t/T = 0.6$, indicating the initial formation of V_d. The birth of V_d is also observed in Fig. 5d at a later instant $t/T = 4/6$. The value of $\langle VP^* \rangle$ becomes more positive and reaches a local maximum at $t/T = 0.9$, reflecting the increasing strength of V_d during the formation stage (as in Fig. 5e). Within $0 < X/C < 0.25$, increasing the magnitude of the local positive maxima of $\langle VP^* \rangle$ indicates a further increase in the strength of V_d. Downstream of $X/C = 0.25$, the magnitude of the local positive maxima decreases gradually, indicating that V_d is lifted away from the surface. The magnitude of $\langle VP^* \rangle$ decreases significantly downstream of $X/C = 0.5$ because V_d has been lifted far away from the airfoil surface and the low-speed flow is dominant in this region.

In Fig. 8, the temporal–spatial variation of the summit-like distribution of $\langle VP^* \rangle$ is found to move at a speed ($1.11U_\infty$) about 8.7% smaller than that of the distorted vorticity field ($1.21U_\infty$) within the region $0 \leq X/C \leq 0.5$. This result correlates well with the slopes of the vortices V_d and V^+ shown in the interacting region of Fig. 6b. Within the region $0 < X/C < 0.5$, the remarkable finding is that the occurrence of the local positive maxima of $\langle VP^* \rangle$ (Fig. 8) has a time lag of $6\%T$ relative to the local negative minima of $\langle \Gamma_l^*(X, t) \rangle$ (Fig. 7). This time-lag clearly reveals that V_d is induced immediately behind the passage of V^-. In Fig. 8 all of the temporal variations of $\langle VP^* \rangle$ are found to correlate well with the formation

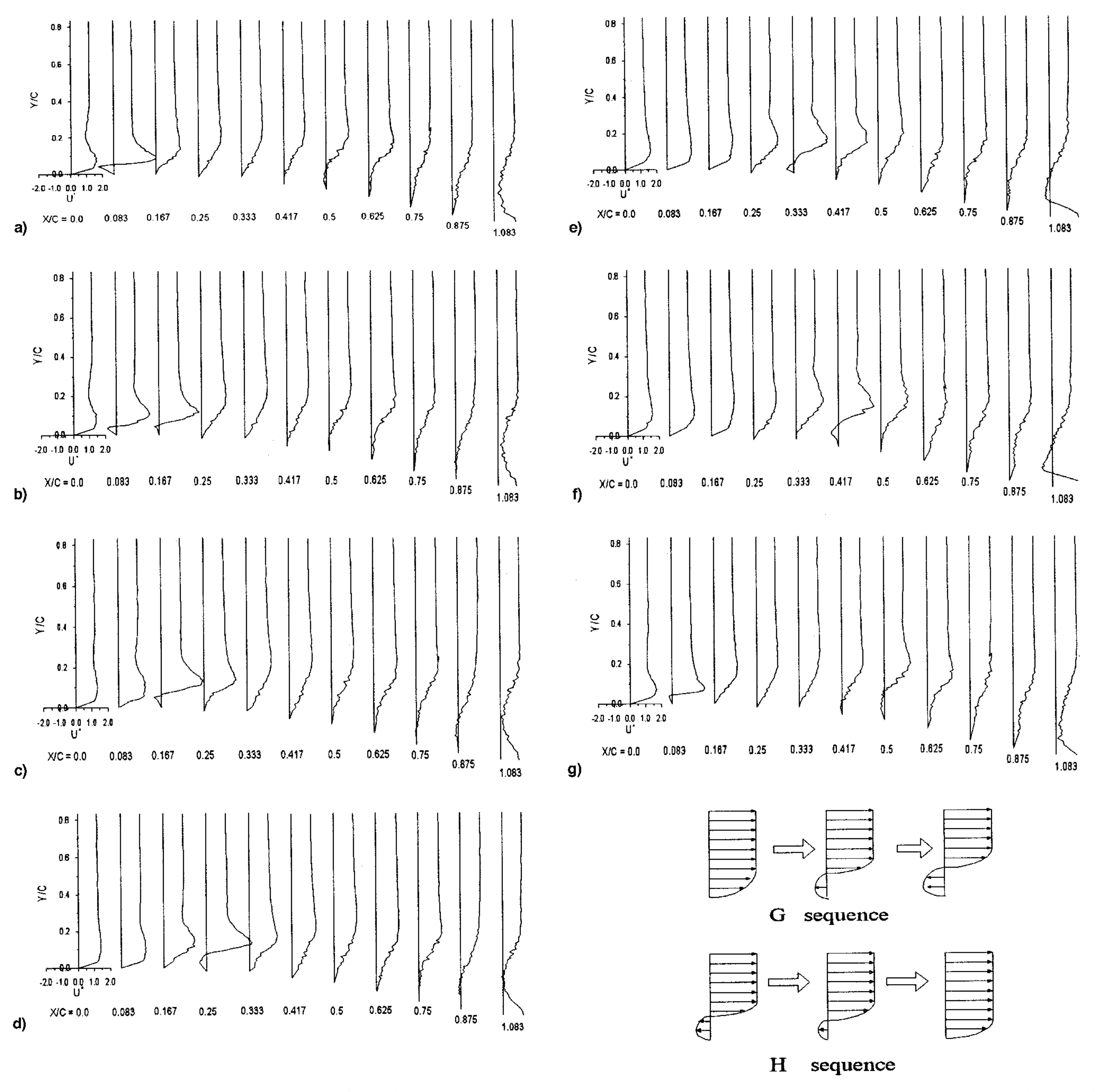

Fig. 9 Phase-averaged velocity profiles [$\langle u(x, y, t) \rangle / U_\infty$] above the airfoil at selected instants within the oscillation cycle. t/T = a) 0.00, b) 0.10, c) 0.22, d) 0.35, e) 0.50, f) 0.66, and g) 0.90.

and the subsequent movement of V_d (Figs. 5b–5e and 6), and is expected to closely relate to the local near-surface flow structures.

Near-Surface Flow Structures

At selected instants within the oscillation cycle, the phase-averaged velocity profiles $\langle u(X, Y, t)\rangle$ over the oscillating airfoil are shown in Fig. 9 to confirm the relationship between the surface vorticity generation $\langle VP^*\rangle$ and the near-surface flow structures over the oscillating airfoil. In Fig. 9, the fuller near-surface velocity profiles at $t/T = 0.22$–0.66 spread over the region $0 \leq X/C \leq 0.083$, indicating the arrival of V^-. At a later instant, $t/T = 0.9$, there exists a flow structure characterized by a reversed flow near the surface, accompanied by a velocity overshoot at the outer region. This flow structure clearly marks the footprints of V_d and V^+. Over the complete oscillation cycle, the previously mentioned flow patterns observed in Fig. 9 imply that V_d is induced immediately behind V^-. Then V_d starts to be lifted by the mutual induction of V^- and V^+, shown in Fig. 5e. Eventually, V_d becomes part of and moves with V^+ along the surface between $X/C = 0.083$ and $X/C = 0.5$. Downstream of $X/C = 0.5$, these flow patterns cannot be observed because V_d has been lifted away from the surface. If the zero-crossing of the reversed velocity profiles can be regarded as the center of V_d, the increasing elevation between the zero-crossing location and the airfoil surface clearly indicates that V_d is lifted away from the surface. This feature is clearly evident in Fig. 9 at $t/T = 0.9$ and $X/C = 0.5$. Over the complete oscillation cycle, the phase-averaged velocity profiles do not show appreciable stalled flow over the airfoil. However, the low-speed flow regime near the airfoil surface dominates at $X/C > 0.5$, and is the primary reason for producing a small amount of vorticity from the local surface in Fig. 8.

In both the spatial and temporal domains, the switch of the near-surface velocity profiles from the G to H sequences of Fig. 9 correlates well with the summit-like variation of $\langle VP^*\rangle$ in Fig. 8. For example, in Fig. 9 at $t/T = 0.1$, the reversed flow pattern occurs within $0.083 < X/C < 0.167$. At the same instant in Fig. 8, the spatial variation of $\langle VP^*\rangle$ does show the summit-like variation at the same streamwise locations. Similar correspondence can also be found at other instants and other streamwise locations in Figs. 8 and 9. The agreement between Figs. 8 and 9 further confirms that the summit-like distributions of $\langle VP^*\rangle$ in the temporal and spatial domains are caused by the formation and subsequent motion of V_d. Furthermore, stronger surface vorticity generation occurs only within the upstroke part of the oscillation cycle.

Overall Circulation Around the Airfoil

During the oscillation cycle different near-surface flow structures may contribute different amounts of vorticity generation from the surface and, thus, the overall circulation $\langle\Gamma_o^*\rangle$ may also be changed. In Fig. 10 $\langle\Gamma_o^*\rangle$ around the airfoil with and without the incident vortex array are compared to reveal the influence of the incident vortex array. The maximum deviation of $\langle\Gamma_o^*\rangle$ estimated over 100 cycles is around 1.47%.

In Figs. 10a and 10b, both cyclic variations of $\langle\Gamma_o^*\rangle$ exhibit the hysteresis character in the counterclockwise direction over the complete oscillation cycle. However, during the oscillation cycle, the amplitudes of the hysteresis differ significantly between these two cases. In the presence of the incident vortex array, the amplitude of the hysteresis appears to be reduced. A large amplitude of the hysteresis implies large differences in the unsteady flow structure during the upstroke and downstroke of the oscillation cycle. When averaged over one complete oscillation cycle, the mean overall circulation is higher with than without the incident vortex array, implying that the incident vortex array has a positive influence to increase the mean overall circulation around the airfoil. In Fig. 9, the phase-averaged velocity profiles show that the flow remains attached over the airfoil surface during the oscillation cycle. Therefore, higher mean overall circulation around the airfoil is the result of a more convex streamline curvature over the airfoil, and vice versa. However, the direct relevance between the hysteresis loop of the overall circulation around and the unsteady loading on the airfoil is not clear at this stage. Details of the surface pressure measurements are needed to further understand this relationship.

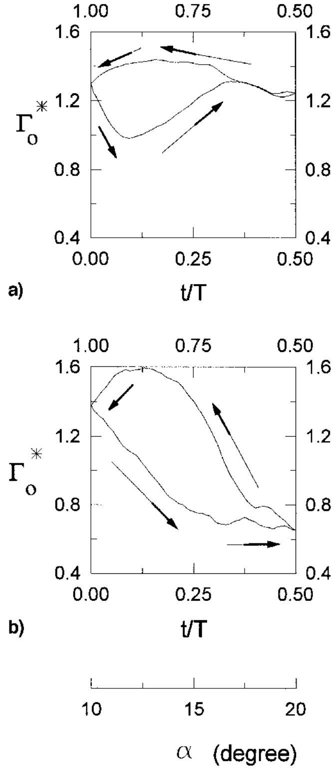

Fig. 10 Cyclic variation of the overall (clockwise) circulation around the oscillating airfoil a) with incident vortex array and b) without incident vortex array.

Concluding Remarks

Parallel interactions of incident vortex array with the oscillating airfoil (NACA 0012) are investigated experimentally, based on the concept of vorticity balance. The phase-averaged velocity field is converted from the single-point LDV velocity measurements and reconstructed by the modified phase-averaged technique. The strength and the convection of the highly distorted vorticity field can be clearly illustrated by the temporal–spatial variations of the local circulation above the airfoil. The phase-averaged near-surface flow structure correlates well with the temporal–spatial variation of the vorticity generation from the airfoil surface, illustrating the formation and subsequent motion of the leading-edge separation vortex along the airfoil. Relative to the negative minima of the local circulation, the summit-like distributions of the vorticity generation are found to lag by about 6% of the oscillating period, implying that the leading-edge separation vortex is induced immediately after the passage of V^-. When compared with the oscillating airfoil in uniform flow, the impingement of the incident vortex array on the oscillating airfoil not only increases the mean overall circulation around the airfoil, but also reduces the amplitude of the hysteresis during the oscillation cycle. During the vortex/airfoil interaction, the formation of V_d, the strength, and the convection of the highly distorted vorticity field over the airfoil are all important characteristics that affect the unsteady airfoil aerodynamics. In the present study these flow characteristics are well documented by the temporal–spatial variations of the local circulation and the local vorticity generation from the airfoil surface.

At the present stage the results of this study are not directly applicable to the vortex/airfoil interaction for the helicopter rotor blade, but will serve as a first step toward the design of experiments intended to understand such interactions. The reduced frequency of the airfoil, the strength and the passage frequency of the incident vortex, as well as the Reynolds number effect are not well scaled with the real applications because of the limitations of the facility. In addition the compressibility and three-dimensional effects are also important and challenging factors that have to be considered in the future. Despite the fact that considerable improvements of the flow conditions are needed to simulate the real applications, the results in this study do reveal the convection of the highly distorted vorticity field and the surface vorticity generation along the airfoil in relation to the phase-averaged velocity field.

Acknowledgment

The authors are grateful for the support of this work by National Science Council of the Republic of China under Contract NSC-84-0424-E-005-003.

References

[1] George, A. R., "Helicopter Noise: State of the Art," *Journal of Aircraft*, Vol. 15, No. 11, 1978, pp. 707–715.

[2] Heller, H., Schultz, K. J., and Amhed, S. R., "Unsteady Surface Pressure Characteristics on Helicopter Blade: A Key to the Physics of Rotor Noise," 19th International Council of the Aeronautical Sciences Congress, Paper 94-2.7.2, Anaheim, CA, March 1994.

[3] Conlisk, A. T., "Modern Helicopter Aerodynamics," *Annual Review of Fluid Mechanics*, Vol. 29, 1997, pp. 515–567.

[4] McCroskey, W. J., "Vortex Wakes of Rotorcraft," AIAA Paper 95-0530, Feb. 1995.

[5] Srinivasan, G. R., Ekaterinaris, J. A., and McCroskey, W. J., "Evaluation of Turbulence Models for Unsteady Flows of an Oscillating Airfoil," *Computers and Fluids*, Vol. 24, No. 7, 1995, pp. 833–861.

[6] Widnall, S., "Helicopter Noise Due to Blade-Vortex Interaction," *Journal of the Acoustical Society of America*, Vol. 50, No. 1, Pt. 2, 1971, pp. 354–365.

[7] Straus, J., Renzoni, P., and Mayle, R. E., "Airfoil Pressure Measurements During a Blade/Vortex Interaction and a Comparison with Theory," *AIAA Journal*, Vol. 28, No. 2, 1990, pp. 222–228.

[8] Booth, E. R., and Yu, C. J., "Two-Dimensional Blade-Vortex Flow Visualization Investigation," *AIAA Journal*, Vol. 24, No. 9, 1986, pp. 1468–1473.

[9] Horner, M. B., Saliveros, E., Kokkalis, A., and Galbraith, M., "Results from a Set of Low Speed Blade-Vortex Interaction Experiments," *Experiments in Fluids*, Vol. 14, No. 5, 1993, pp. 341–352.

[10] Srinivasan, G. R., and Baeder, I. D., "TURNS: A Free Wake Euler-Navier-Stokers Numerical Method for Helicopter Rotors," *AIAA Journal*, Vol. 31, No. 5, 1993, pp. 959–962.

[11] Mook, D. T., and Dong, B., "Perspective: Numerical Simulation of Wakes and Blade-Vortex Interaction," *Journal of Fluids Engineering*, Vol. 116, No. 1, 1994, pp. 5–21.

[12] Carr, L. W., and McCroskey, W. J., "A Review of Recent Advances in Computational and Experimental Analysis of Dynamic Stall," *International Union of Theoretical and Applied Mechanics Symposium on Fluid Dynamics of High Angle of Attack* (Tokyo, Japan), Springer–Verlag, New York, 1992, pp. 3–32.

[13] Gopalkrishnan, R., Triantafyllou, M. S., Triantafyllou, G. S., and Barrett, D., "Active Vorticity Control in a Shear Flow Using Flapping Foil," *Journal of Fluid Mechanics*, Vol. 274, 1994, pp. 1–21.

[14] Koochesfahani, M. M., "Vortical Patterns in the Wake of an Oscillating Airfoil," *AIAA Journal*, Vol. 27, No. 9, 1989, pp. 1200–1205.

[15] Kuo, C. H., and Hsu, C. W., "Development of Vortical Structure over Delta Wing with Leading-Edge Flap," *Journal of Aircraft*, Vol. 34, No. 5, 1997, pp. 577–584.

[16] Hsieh, J. K., "Experimental Investigations on the Incident Vortex Array Interactions with the Oscillating Airfoil," M.S. Thesis, Dept. of Mechanical Engineering, National Chung-Hsing Univ., Taiwan, ROC, 1997.

[17] Ho, C. M., and Nosseir, N. S., "Dynamics of an Impinging Jet. Part I:. Feedback Phenomena," *Journal of Fluid Mechanics*, Vol. 105, 1981, pp. 119–142.

[18] Shih, C., and Ho, C. M., "Vorticity Balance and Time Scales of Two-Dimensional Airfoil in an Unsteady Free Stream," *Physics of Fluids, Series A*, Vol. 6, No. 2, 1994, pp. 710–723.